

Finite-size effects on molecular dynamics interfacial thermal-resistance predictionsZhi Liang^{1,*} and Pawel Koblinski^{1,2,†}¹*Rensselaer Nanotechnology Center, Rensselaer Polytechnic Institute, Troy, New York 12180, USA*²*Department of Materials Science and Engineering, Rensselaer Polytechnic Institute, Troy, New York 12180, USA*

(Received 19 May 2014; revised manuscript received 4 August 2014; published 15 August 2014)

Using molecular dynamics simulations, we study the role of finite size effects on the determination of interfacial thermal resistance between two solids characterized by high phonon mean free paths. In particular, we will show that a direct, heat source-sink method leads to strong size effect, associated with ballistic phonon transport to and from, and specular reflections at the simulation domain boundary. Lack of proper account for these effects can lead to incorrect predictions about the role of interfacial bonding and structure on interfacial thermal resistance. We also show that the finite size effect can be dramatically reduced by introduction of rough external boundaries leading to diffuse phonon scattering, as explicitly demonstrated by phonon wave-packet simulations. Finally, we demonstrate that when careful considerations are given to the effects associated with the finite heat capacity of the simulation domains and phonon scattering from the external surfaces, a size-independent interfacial resistance can be properly extracted from the time integral of the correlation function of heat power across the interface. Our work demonstrates that reliable and consistent values of the interfacial thermal resistance can be obtained by equilibrium and nonequilibrium methods with a relatively small computational cost.

DOI: [10.1103/PhysRevB.90.075411](https://doi.org/10.1103/PhysRevB.90.075411)

PACS number(s): 65.40.-b, 66.70.-f, 63.22.-m

I. INTRODUCTION

Heat flow across the interface between two materials leads to a discontinuous temperature drop at the interface which is quantified by the interfacial thermal resistance (Kapitza resistance) [1] R_K . Due to the high surface-to-volume ratio in nanostructured components in microelectronics and advanced energy systems, the thermal resistance at material interfaces often dominates the overall thermal resistance of nanostructured components. On one hand, this phenomenon can be utilized, for example, in thermoelectric devices to enhance the thermal to electrical energy conversion efficiency [2,3]. On the other hand, it can also cause a local overheating problem leading to low efficiency or even failure in microelectronics [4]. To fulfill the thermal management requirements in different microdevices, various interface engineering techniques have been proposed to tune R_K at material interfaces [2–11].

In exploration of the interfacial structure–thermal transport property relationship, molecular dynamics (MD) simulations are often used, as in such simulations one can create and characterize well-controlled interfaces at the atomic level. Moreover, the MD simulation method is ideally suited to study thermal transport in nanosized semiconductor devices since phonons are the primary thermal energy carriers in most semiconductors and MD simulations require no assumption about the nature of the phonon scattering.

In MD simulations R_K can be computed either using nonequilibrium MD (NEMD) or equilibrium MD (EMD). The standard NEMD method imposes a steady heat flux across the material interface. By contrast, the EMD method uses the fluctuations of heat power across the interface to compute R_K via the fluctuation-dissipation theorem and the Green-Kubo formula [12–16].

Previous studies have shown that the EMD and NEMD methods give consistent results of R_K at solid-liquid and solid-gas interfaces [12–14]. However, controversial results were obtained when the EMD method was used to calculate R_K at solid-solid interfaces. Chalopin *et al.* [16] computed R_K via EMD at an isolated epitaxial Si|Ge interface formed by two 10-nm slabs at 400 K. They claimed that their result is consistent with NEMD results in the literature. However, it was not clear from their work if the EMD prediction of R_K at an isolated interface is affected by the finite system size or not. The size effects issue was addressed by Merabia and Termentzidis [15] who studied an interface between two Lennard-Jones (LJ) crystals, and demonstrated strong system size effects for the EMD method. In particular, depending on the mass mismatch between two LJ solids, they found that R_K 's predicted from EMD and NEMD methods could differ by a factor of 4 to 10.

The finite size effect in NEMD simulations is a well-known problem in R_K determination. A number of studies have shown that R_K is size dependent if the thickness of the two materials forming the interface is comparable to the bulk phonon mean free path (MFP) [17–20]. It is notable that the size-dependent R_K was also observed in experiment on contact thermal resistance between multiwalled carbon nanotubes, where it was shown that resistance normalized by the contact area depends on the number of walls [21].

Our recent modeling and simulation study on thermal transport across an interface between thin film and the substrate has shown that the size effect on R_K is a combined effect of internal and boundary scattering of phonons [20]. In particular, when the thickness of materials forming the interface is less than the bulk phonon MFP, the phonons transmitted from material 1 to material 2 have a high probability to travel ballistically in material 2. If these phonons are not diffusely scattered by the external surfaces or the heat source/sink, they can be specularly reflected and transmitted back to material 1 without energy transfer. This effectively reduces the phonon

*liangz3@rpi.edu

†keblip@rpi.edu

transmission coefficient and increases R_K . Therefore, R_K not only depends on the thickness of materials forming the interface, but also depends on how phonons scatter at the external surface of thin films or in the heat source and heat sink regions.

The rest of the paper is organized as following: In Sec. II we introduce a model system, describe heat sink-source simulation methodology, and present simulation results emphasizing finite size effects and their dependence on the structure of the simulation domain boundary. We will also discuss the potential and limitations of imposing diffuse scattering by using Langevin thermostats to implement the heat source and sink scheme. In Sec. III we describe the wave-packet simulation procedure and frequency dependent phonon scattering characteristics at the internal and external interfaces. In Sec. IV we will analyze the finite size effect on EMD prediction of R_K and demonstrate consistency between the EMD and NEMD simulation results. Finally, we will present a summary and conclusions.

II. NEMD PREDICTION OF R_K

A. The MD model

The model system used in our studies is the interface formed by a GaN lead and an AlN lead. In this model both GaN and AlN have a Wurtzite hexagonal crystal structure. As shown in Fig. 1, the $[1\bar{1}00]$, $[11\bar{2}0]$, and $[0001]$ directions of the GaN and AlN crystals are aligned, respectively, in the x , y , and z directions of the simulation box. The atomic interactions are modeled using the Stillinger-Weber (SW) potential with parameters developed by Bere and Serra [22] (for GaN) and Lei [23] (for AlN). To be consistent with the potential parameters developed by Lei [23], only the nearest neighbor interactions are considered in the simulation, such that there is no Ga-Al pair interaction. The three body Ga-N-Al term is computed

based on the geometric mean of the values for the two bonds. Using these SW potentials, MD simulations predict that the lattice constants are $a = 3.19 \text{ \AA}$, $c = 5.22 \text{ \AA}$ for GaN and $a = 3.09 \text{ \AA}$, $c = 5.05 \text{ \AA}$ for AlN [20]. Thus, consistent with experimental data, there is a $\sim 3.2\%$ lattice mismatch between the GaN and AlN crystals.

We first consider an epitaxial GaN|AlN interface. To make AlN and GaN crystals commensurate, we strain the cross section of the GaN crystal in the x and y directions. For this structure we define a unit orthogonal cell whose dimensions in the x , y , and z directions are, respectively, $2a \cos(\pi/6)$, a , and c . The simulation box has a cross section area of 3 unit cells in the x direction by 5 unit cells in the y direction. Periodic boundary conditions (PBCs) are applied in the x and y directions. Simulations were also performed on a system 4 times larger in the cross section area, and only $\sim 2\%$ difference in interfacial conductance was observed. Hence, the cross section area of 3×5 unit cells is large enough to remove the possible size effect related to the finite cross section area. The GaN lead and AlN lead contain the same number of unit cells in the z direction. At the two edges of the simulation box, there are 10-unit-cell long heat source and heat sink regions and free boundaries. The length of the system is varied to study the finite size effect on R_K .

All simulations are performed at 300 K and zero stress in the z direction, while the x and y dimensions are kept fixed. A velocity Verlet algorithm with a time step size of 1 fs is used for the integration of equations of motions [24]. Prior to each MD simulation run, we do energy minimization of the structure at 0 K to remove the artificial mechanical stresses present in an as-prepared heterogeneous system. The system is then equilibrated at 300 K for 1 ns. After the system reaches thermal equilibrium, the global thermostat is turned off, and a heat flux of 5 GW/m^2 is applied by adding a constant amount of energy to the heat source and removing the same amount of energy from the heat sink at each time step using the velocity rescaling method [25]. Each simulation run is carried out for 6 ns to allow the system to reach a steady state, and then for additional 50 ns for data collection and averaging. We also performed simulations with a higher heat flux of 7.5 GW/m^2 , the value of interfacial conductance differs by less than 2%. Hence, there are no effects of heat flux or temperature drop at the interface in our simulation.

The NEMD simulation determines Kapitza resistance R_K by

$$R_K = \Delta T/q, \quad (1)$$

where ΔT is the temperature drop at the interface and q is the heat flux across the interface. In NEMD simulation we calculate the bin-by-bin temperature profile with the bin width of 5 unit cells in the heat flow direction. The temperature drop ΔT is determined by linear extrapolation of the temperature profiles in the two leads to the interface. The uncertainties are determined from the analysis of four independent simulation runs.

B. Surface roughness dependence of R_K

We first determine the $R_{K,\infty}$ which characterizes smooth surfaces in the limit of the infinite system length. According to

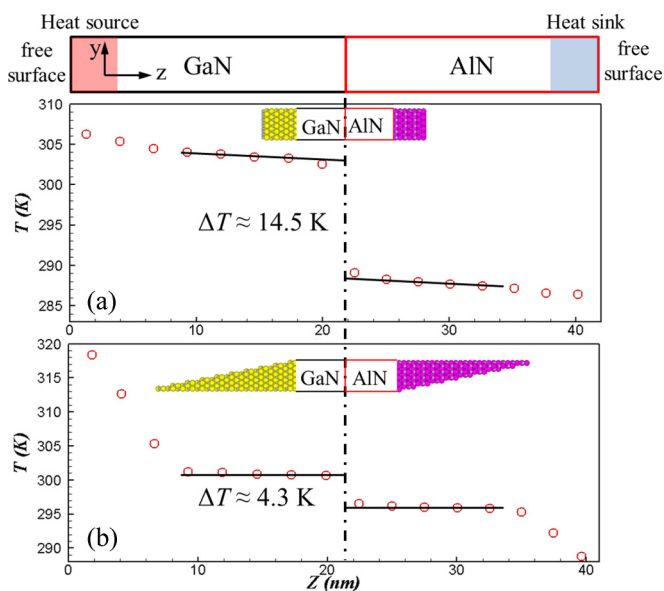


FIG. 1. (Color online) Schematic diagram of the simulation box and the corresponding temperature profiles in the NEMD simulation. (a) Smooth and (b) very rough external surfaces.

standard practice of studying the size dependence of R_K , we gradually increase the length of each lead from 40 unit cells to 150 unit cells and calculate R_K at each length. Figure 1(a) shows the temperature profile of the smallest system size (40|40 unit cells). At such a system size, the temperature drop at the interface $\Delta T = 14.5 \pm 0.3$ K and the Kapitza resistance $R_K = 2.90 \pm 0.04$ m² K/GW. As the system length increases, R_K decreases monotonically to 1.36 ± 0.05 m² K/GW at the length of 150|150 unit cells. By extrapolating R_K to an infinite system length limit, the system with smooth external surfaces predicts $R_{K,\infty} \approx 0.82$ m² K/GW. Accordingly, the Kapitza conductance in the limit of large system length, $G_{K,\infty}$ ($= 1/R_{K,\infty}$) ≈ 1.22 GW/m² K. As a comparison, the experimental value of G_K at GaN|AlN interface, which was derived from thermal conductivity measurement of (AlN)_{4.1 nm}-(GaN)_{55 nm} superlattices, was found to be about 0.62 GW/m² K [26]. It was pointed out by Koh *et al.* that the GaN|AlN interface in their experiment might not be perfectly smooth and G_K could be larger for smoother interfaces. Using the acoustic mismatch model, Koh *et al.* estimated G_K at a smooth GaN|AlN interface is 1.4 GW/m² K [26]. Therefore, the G_K predicted by NEMD simulations is in reasonable agreement with the experimental values and the theoretical prediction.

A similar size dependence of R_K was also found in the literature for systems with fixed boundaries [17,18] and with PBCs [19] in the heat flow direction. As we discussed in our previous work [20], the relatively large R_K at small system sizes is mainly caused by specular reflection of ballistic phonons at the smooth external surfaces which leads to the reduction of the effective phonon transmission coefficient. The specularity p of the external surface can be estimated from the Soffer's model [27]

$$p(k) = \exp(-k^2 h^2), \quad (2)$$

where k is the wave vector of the phonon and h is the surface roughness. For an atomistically smooth surface, $h \approx 0$, the Soffer's model predicts $p(k) = 1$, which indicates all phonons will be scattered specularly. In another extreme case when $h \rightarrow \infty$, Eq. (2) predicts $p(k) = 0$, which means all phonons will be diffusely scattered at the external surface. To investigate how R_K depends on external surface roughness, we fix the system length at 40|40 unit cells and gradually increase the roughness of external surfaces. The rough external surface is generated in the MD model by removing half of the atoms in the region ranging from 0 to dz from the surface as shown in the inset of Fig. 2. The ratio dz/dy ($dy \approx 1.6$ nm) is tuned from 0 to 5 to increase the surface roughness.

The temperature profile of the system with the biggest roughness ($dz/dy = 5$) is shown in Fig. 1(b). It is evident from Fig. 1 that with such a rough external surface ΔT is about a factor of 3 smaller than that with a smooth external surface. The result manifests that R_K at the internal interface is strongly affected by the external surface roughness.

Figure 2 shows the variation of G_K with the increase of external surface roughness. If the surface roughness h is relatively small ($dz/dy < 4$), the rough surface can scatter short-wavelength (greater wave vector k) phonons diffusely, but long-wavelength phonons (smaller wave vector, k) specularly. Therefore, a rougher surface reduces the specular reflection of phonons and increases G_K . When the external surface

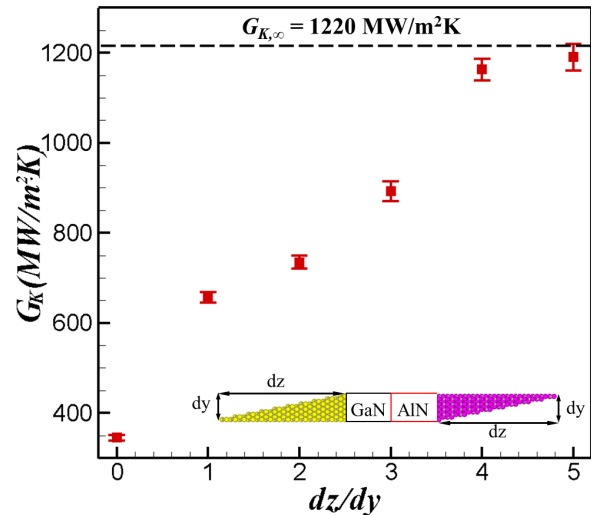


FIG. 2. (Color online) Kapitza conductance G_K as function of roughness of external surfaces. The inset shows the structure of the rough external surface. The surface roughness increases with the ratio dz/dy . The horizontal dashed line indicates the value of $G_{K,\infty}$.

becomes very rough ($dz/dy \geq 4$), the majority of transmitted phonons will be diffusely scattered. A further increase of surface roughness can help diffusely scatter phonons of very long wavelengths. However, due to the very small population of these phonons, their contribution to the interfacial thermal transport is limited. According to Fig. 2, the G_K for very rough surfaces ($dz/dy \geq 4$) is essentially roughness independent and is close to $G_{K,\infty}$ which characterizes smooth surfaces in the limit of infinite system length.

C. R_K at a nonepitaxial interface

While phonon scattering at perfect epitaxial interfaces is essentially nondiffuse [17,20], the interface scattering is at least partially diffuse at nonepitaxial interfaces and grain boundaries [28,29]. To investigate the effect of diffuse interface scattering on MD prediction of R_K , we compute R_K at a nonepitaxial GaN|AlN interface using NEMD simulations.

To accommodate the 3.2% lattice mismatch, the cross section of GaN and AlN leads contains, respectively, 31×31 unit cells and 32×32 unit cells. Figure 3(a) shows the cross section structure of the nonepitaxial GaN|AlN interface. It is seen from Fig. 3(a) that the lattice mismatch leads to atomic restructuring and dislocations at the interface. This structure makes the interface scattering more diffuse.

Similarly to the procedure described in the previous sections, we vary the system length from 40|40 unit cells to 150|150 unit cells and use NEMD simulations to determine the R_K (nonepitaxial). The result of R_K (nonepitaxial) as a function of $1/L$ where L is total system length is shown in Fig. 4. As a comparison, the size dependent R_K (epitaxial) is also shown in Fig. 4.

It is evident from Fig. 4 that with smooth external surfaces, the size effect on R_K (nonepitaxial) is smaller than that on R_K (epitaxial). By linear extrapolating R_K (nonepitaxial) to infinite system length, it is shown in Fig. 4 that $R_{K,\infty}$ (nonepitaxial)

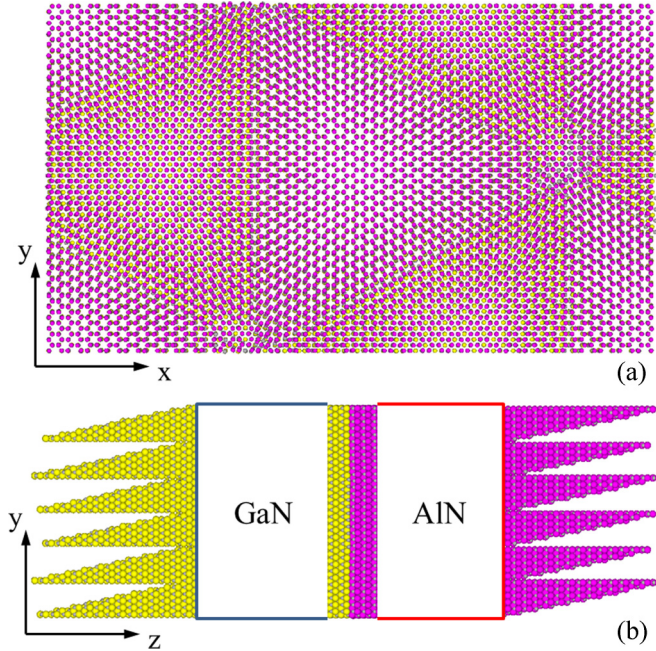


FIG. 3. (Color online) (a) The cross section structure of the nonepitaxial GaN|AlN interface. (b) The structure of very rough external surfaces when GaN and AlN form a nonepitaxial interface.

is $\sim 1.23 \text{ m}^2 \text{ K/GW}$ which is 50% higher than $R_{K,\infty}(\text{epitaxial})$. The smaller size effect and greater $R_{K,\infty}$ at the nonepitaxial interface are both caused by diffuse interface scattering.

For diffuse interface scattering, the phonon transmission coefficient can be estimated by the diffuse mismatch model (DMM) [30] which relates the transmission coefficient to

phonon density of states (DOS) on both sides of the interface. GaN and AlN crystals have similar Debye temperatures [31] leading to good overlap of the phonon spectra. In this case, DMM predicts the transmission coefficient $\tau \approx 0.5$, which is much smaller than the value of $\tau \approx 1$ predicted by the acoustic mismatch model (AMM) [30] at the perfect epitaxial interface. Our previous study shows that the size effects are maximized when the phonon transmission coefficient is very high [20]. The nonepitaxial interface scatters phonons more diffusely and has a lower phonon transmission coefficient. Hence, it is reasonable to see a higher $R_{K,\infty}$ and smaller size effect on R_K at the nonepitaxial interface.

In spite of the fact that $R_{K,\infty}(\text{nonepitaxial})$ is higher than $R_{K,\infty}(\text{epitaxial})$, it is notable in Fig. 4 that $R_K(\text{nonepitaxial})$ could be lower than $R_K(\text{epitaxial})$ if the system size is small. This result suggests caution in interpreting MD simulation results of R_K where the system size is not long enough to eliminate the size effect. Due to the size effect, opposite conclusions could be drawn at different system lengths.

As shown in the previous sections, the size effect can be essentially eliminated by introducing very rough external surfaces. Hence, as shown in Fig. 3(b), we generate very rough surfaces ($dz/dy = 5$) in two leads that form the nonepitaxial interface. Similar to what we found for the epitaxial interface, $R_K(\text{nonepitaxial})$ involving very rough external surface is essentially independent of L (see Fig. 4). Since the size effect is greatly eliminated, $R_K(\text{nonepitaxial})$ is consistently higher than $R_K(\text{epitaxial})$, regardless of the system size. To get the same conclusion from simulations with smooth surfaces, however, one needs to increase the system size to 150|150 unit cells as shown in Fig. 4. It is also shown in Fig. 4 that there is a nice agreement of the infinite system extrapolations for the epitaxial systems with smooth and rough interfaces. However, this agreement is not seen for the nonepitaxial interface. The result indicates the linear relation between $R_K(\text{nonepitaxial})$ and $1/L$ cannot be extended to very large system sizes. Similar phenomena were also found at GaN|Al interfaces by Jones *et al.* [18]. The explanation to such phenomena requires separate work.

D. Effect of thermostat in heat source/sink

In the previous NEMD simulations we used the velocity rescaling method [25] in the heat source/sink to generate constant heat flux across the interface. The highly size-dependent R_K indicates that this thermostat does not lead to significant diffuse scattering. We also showed that diffuse phonon-boundary scattering can eliminate the size effect. This raises a question of the possibility to eliminate the size effect on R_K by employing a thermostat that can diffusely scatter phonons reaching the heat source/sink.

To explore this issue we employ Langevin thermostats in the heat source/sink. In Langevin dynamics, the temperature is maintained by modifying Newton's equations of motion according to Eq. (3) [32]:

$$\vec{r}_i = \vec{p}_i/m_i, \quad \frac{d\vec{p}_i}{dt} = \vec{F}_i - \gamma_i \vec{p}_i + \vec{f}_i, \quad (3)$$

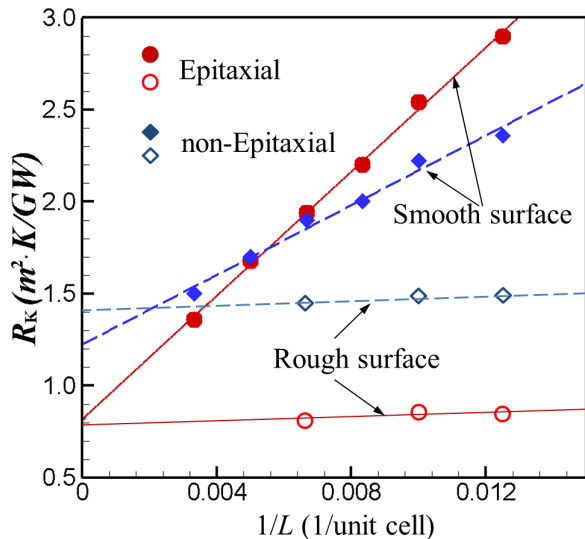


FIG. 4. (Color online) R_K as a function of $1/L$ for an epitaxial interface involving smooth external surfaces (filled circles), an epitaxial interface involving very rough external surfaces (open circles), a nonepitaxial interface involving smooth external surfaces (filled diamonds), and a nonepitaxial interface involving very rough external surfaces (open diamonds). The lines show fitting of the data by linear functions.

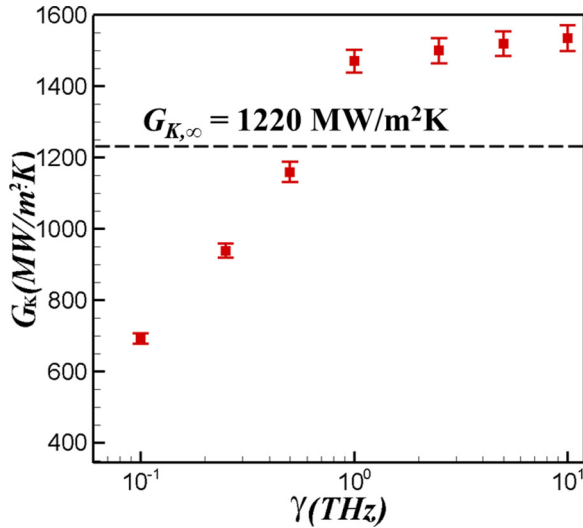


FIG. 5. (Color online) G_K as a function of friction coefficient γ in the Langevin thermostat. The horizontal dashed line indicates the value of $G_{K,\infty}$.

where r_i , p_i , and m_i are, respectively, position, momentum, and mass of atom i , t represents time, F_i is the force acting on atom i due to the interaction potential, γ_i is a friction coefficient, and f_i is a random force determined from a Gaussian distribution with dispersion σ_i related to γ_i via

$$\sigma_i^2 = 2m_i\gamma_i k_B T / \Delta t, \quad (4)$$

where k_B is the Boltzmann constant, and Δt is the time step size used in MD simulation.

By increasing the friction coefficient γ in the Langevin thermostat, the magnitude of the friction force and random force increase, which leads to more diffuse phonon scattering in the heat source/sink. To investigate how this diffuse thermostat affects the MD prediction of R_K , we gradually increase γ from 0.1 to 10 THz and compute R_K at an epitaxial interface. Smooth external surfaces are used in the simulation. The system length is fixed at 40|40 unit cells and the heat source and heat sink temperatures are set to 305 and 287 K, respectively. By monitoring energy input to the heat source and sink, we determine the time averaged heat power and the heat flux. All other settings are the same as those in the previously described MD simulations.

In Fig. 5 we show interfacial conductance G_K as a function of the friction coefficient γ . As γ increases, phonon scattering becomes more diffuse in the heat source/sink, which reduces the number of phonons specularly reflected at the surface. Accordingly, it is seen in Fig. 5 that G_K increases with γ . This phenomenon is similar to the increase of G_K with surface roughness shown in Fig. 2. When γ is high, the heat source/sink can scatter the majority of phonons diffusely. Hence, one may expect that G_K at high γ 's will be close to $G_{K,\infty}$ that characterizes smooth surfaces in the limit of infinite system length. However, it is evident from Fig. 5 that G_K at high γ 's does not approach $G_{K,\infty}$, but to a higher value.

To explain the discrepancy, we calculate vibrational DOS (VDOS) in GaN by the Fourier transform of the velocity

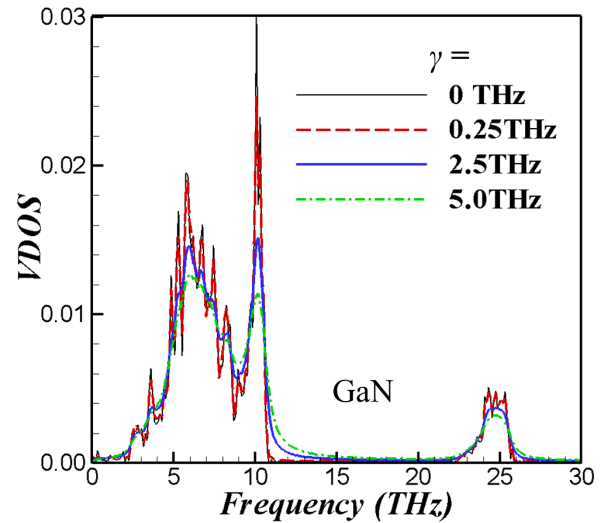


FIG. 6. (Color online) VDOS of Ga atoms in GaN in the case of friction coefficient $\gamma = 0, 0.25, 2.5,$ and 5 THz.

autocorrelation function (VAF) [33]:

$$C(\omega) = \int_0^\infty \langle \bar{v}(t) \bar{v}(0) \rangle e^{i\omega t} dt, \quad (5)$$

where $C(\omega)$ is the VDOS at frequency ω , $\langle \dots \rangle$ means ensemble average, and v is the atomic velocity. The VAF is determined from the EMD simulation at constant temperature. The GaN crystal is maintained at 300 K in the simulation by Langevin thermostat with different γ 's. The resulting VDOS of Ga atoms is shown in Fig. 6. The calculated VDOS ($\gamma = 0$) is in reasonable agreement with the experimental measurements [34,35] for low-frequency modes. However, a substantial difference between the calculated and experimental VDOS is found for the high-frequency optical modes. As pointed out by Zhou *et al.* [36], the difference is mainly due to the fact that the long-range electrostatic interaction is not included in the SW potential.

When γ is small such as $\gamma = 0.25$ THz in Fig. 6, the VDOS are essentially the same as that obtained in a microcanonical ensemble ($\gamma = 0$). If γ is large such as $\gamma = 2.5$ and 5 THz in Fig. 6, the VDOS evidently deviates from that at $\gamma = 0$. In this case, unrealistic phonon distributions will be generated in the heat source/sink. When the system length is small, these phonons can travel ballistically from the heat source/sink to the interface, which influences the correct prediction of G_K . Since G_K is highly γ dependent and does not converge to $G_{K,\infty}$, we conclude that reliable prediction of R_K in a system with small length cannot be easily achieved by employing Langevin thermostat in the heat source/sink. A better result can be perhaps obtained with a smaller γ but much larger (spatially) thermostat regions allowing for diffuse scattering. However, this will require larger sizes and systematic studies of the role of thermostated region size and γ . By contrast, introduction of the rough surfaces described in the previous section appears to be much more robust and efficient methods to suppress the size effects.

E. Temperature profiles of low- and high-frequency modes

In this section we gain further insights in the coupling between interfacial and boundary scattering. We analyze the size effect on interfacial phonon transport for phonons of low- and high-frequency modes. This analysis relies on computing temperature profiles of low- and high-frequency phonon modes in GaN and AlN leads that form an epitaxial interface.

In the previous section we calculated VDOS $C(\omega)$ at 300 K. In fact, the unnormalized $C(\omega)$ is proportional not only to the number of vibrations per unit frequency but also to the absolute temperature [37]. Therefore, a frequency-dependent temperature of an atom can be defined as [37]

$$T(\omega) = T_{eq} \frac{\int_{\omega}^{\omega+\Delta\omega} C_{ne}(\omega')d\omega'}{\int_{\omega}^{\omega+\Delta\omega} C_{eq}(\omega')d\omega'}, \quad (6)$$

where $C_{eq}(\omega)$ and $C_{ne}(\omega)$ represent VDOS functions for equilibrium and nonequilibrium thermally driven systems, and $T_{eq}(300\text{ K})$ is the temperature of the equilibrium system. Based on $C_{eq}(\omega)$ ($\gamma = 0$) shown in Fig. 6, the temperatures of low- and high-frequency modes are defined via Eq. (6) with integrals taken from, respectively, 2 to 11 THz and 23 to 27 THz.

Figure 7(a) shows the temperature profiles of low- and high-frequency modes in a 40|40-unit-cell long system with smooth external surfaces. It is seen in Fig. 7(a) that the temperature drop at the interface for low-frequency modes is much larger than that for high-frequency modes. The large difference between the two temperature drops is caused by

the small size of the structure. As the external surfaces of the structure are smooth, the phonon-phonon scattering in the two leads are the main scattering mechanism. The bulk MFP of low-frequency phonons is normally much longer than that of high-frequency phonons [38]. Hence, the transmitted low-frequency phonons have a high possibility of traveling ballistically in the lead and returning to the interface without being scattered diffusely. Accordingly, the effective transmission coefficient of low-frequency phonons is much lower than that of high-frequency phonons. With the increase of the system size, more low-frequency phonons are scattered diffusely in the lead and their effective transmission coefficient increases. When system size increases to 75|75 unit cells, the probability of bulk scattering increases and the temperature profiles for both frequency ranges become similar. These results clearly show that the size effect on interfacial phonon transport is highly frequency dependent.

It is also seen in Fig. 7 that the difference between high-frequency temperature and low-frequency temperature in the GaN lead is bigger than that in the AlN lead. This is mainly caused by the much longer phonon MFP in AlN. It was found in our previous work [20] that the average phonon MFP is about 52 nm in GaN and 127 nm in AlN at 300 K. As the average MFP is much shorter in GaN, the phonons transmitted to GaN have a higher possibility to be scattered diffusely in the GaN. Accordingly, less transmitted phonons will travel ballistically in GaN and return to AlN without being scattered diffusely. Hence, the effective transmission coefficient from AlN to GaN is larger than that from GaN to AlN. That is the reason why

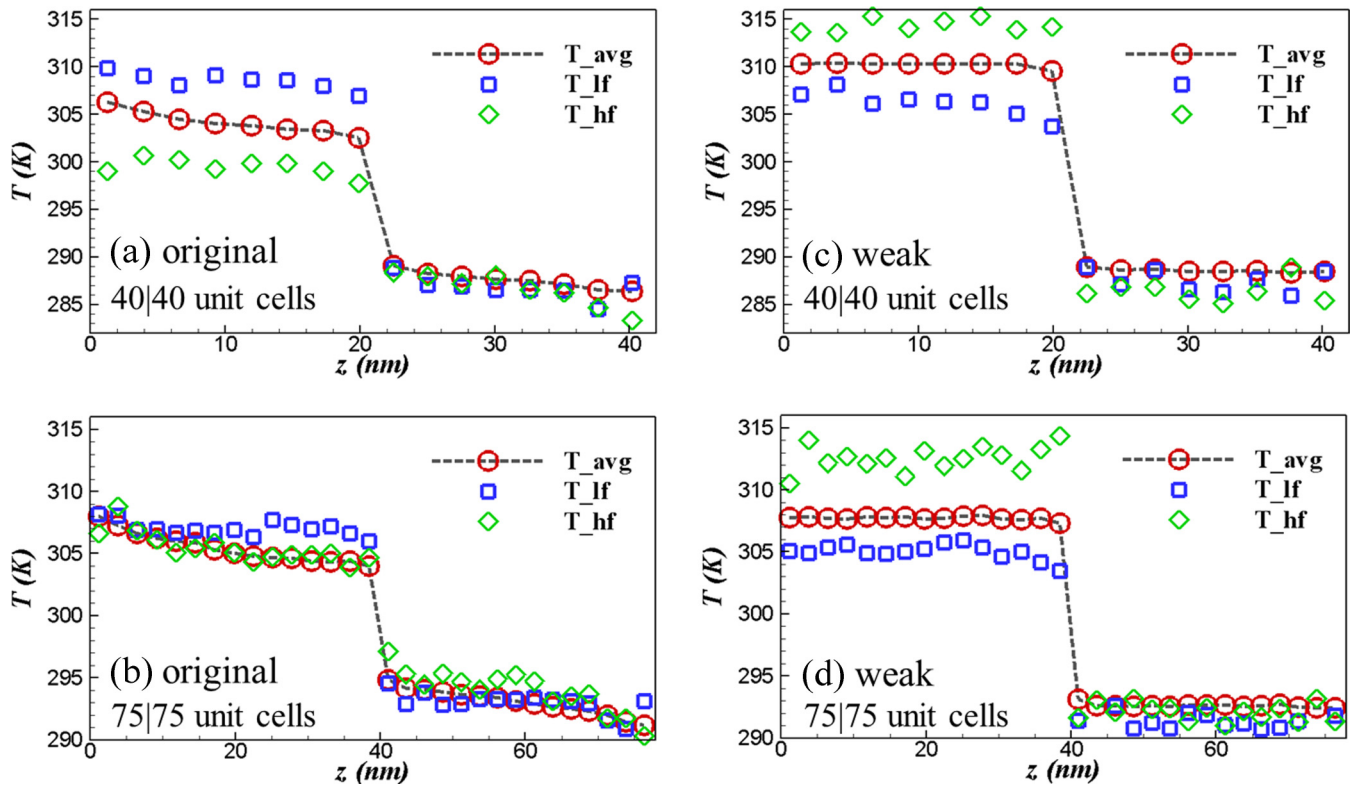


FIG. 7. (Color online) Temperature profiles of low- (2–11 THz) and high- (23–27 THz) frequency phonon modes and all phonon modes in (a) 40|40-unit-cell structure, (b) 75|75-unit-cell structure, (c) 40|40-unit-cell structure with weak interface interactions, and (d) 75|75-unit-cell structure with weak interface interactions.

the temperature difference between different phonon modes is smaller in the AlN lead.

The above results are obtained in a system with a high transmission coefficient at the interface. In the following we compute frequency-dependent temperature profiles in a system with much lower transmission coefficient. To reduce the transmission coefficient we multiply the interaction potential and force between atoms on the two sides of the interface by a factor of 0.05. The weak interaction significantly lowers the interfacial thermal conductance. To avoid too large of a temperature drop at the interface, the heat flux applied in the simulation is reduced to 0.5 GW/m².

While the weak interface interaction greatly limits the transmission of high-frequency phonons, the low-frequency acoustic phonons are not affected by the weak interaction at the interface due to their long wavelength. The long-wavelength acoustic phonons only recognize the bulk properties of the two materials. Hence, the transmission coefficient of low-frequency acoustic phonons is still high [9,39]. Accordingly, it seen in Fig. 7(c) that the temperature drop at the weakly bonded interface for low-frequency modes is much lower than that for high-frequency modes. A similar result is seen in Fig. 7(d) where the system size is increased from 40|40 unit cells to 75|75 unit cells. At the weakly bonded interface, the big difference in the temperature drops between low- and high-frequency modes is not due to the difference in the size effect, as in the case of strong-interaction interface, but mainly due to the big difference in the interfacial transmission coefficients.

III. WAVE-PACKET SIMULATION OF PHONON-BOUNDARY SCATTERING

In this section we present the results of wave-packet simulations to explicitly demonstrate the effects of surface roughness on phonon-boundary scattering and phonon transport across the epitaxial GaN|AlN interface.

First we calculate phonon spectra including eigenvalues and eigenvectors by diagonalizing the dynamical matrix of the cross section strained GaN crystal and the perfect AlN crystal that form the epitaxial GaN|AlN interface. To determine the harmonic force constants in the dynamical matrix, we displace the atoms in the fully relaxed structure by $\pm 10^{-5}$ Å from the equilibrium position in three directions and the force constants are obtained from the second order derivatives of potential energy. Since GaN and AlN have a Wurtzite hexagonal crystal structure whose primitive cell contains four atoms, there are 12 phonon branches in each crystal. Figures 8(a) and 8(b) show dispersion curves along [0001] direction in strained GaN and AlN, respectively.

To generate a phonon wave packet centered at a wave vector k_0 in λ branch, and localized in space around z_0 with a spatial extent of $\sim 1/\eta$, we displace the atoms according to [40]

$$u_l^\alpha(s) = \frac{1}{\sqrt{M_s}} Q_{\lambda k_0} \varepsilon_{\lambda k_0}^\alpha(s) e^{ik_0(z_l - z_0)} e^{-\eta^2(z_l - z_0)^2}, \quad (7)$$

where $u_l^\alpha(s)$ represents α component of displacement of atom s in primitive cell l , M_s is the mass of atom s , $Q_{\lambda k_0}$ is the amplitude of the wave, $\varepsilon_{\lambda k_0}^\alpha(s)$ is the α component of eigenvector of atom s for λ branch at k_0 , and z_l is the z

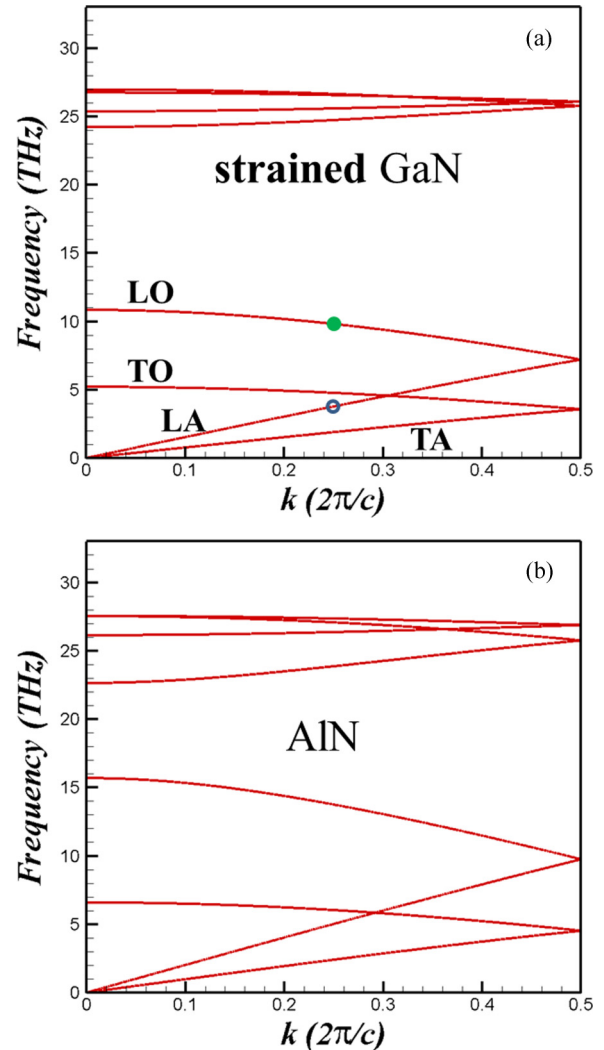


FIG. 8. (Color online) The dispersion curve for [0001] phonons of (a) cross section strained GaN and (b) AlN. The open circle in (a) indicates the 3.769-THz LA mode phonon in strained GaN. The filled circle in (a) indicates the 9.807-THz LO mode phonon in strained GaN.

coordinate of the primitive cell l . In the simulation we set $Q_{\lambda k_0} = 10^{-5}$ Å and $1/\eta = 25$ unit cells. To form a wave packet that is localized in both real space and wave vector space as described in Eq. (7), the initial atomic displacements are expressed in terms of linear combination of vibrational eigenstates [28]

$$u_l^\alpha(s) = \frac{1}{\sqrt{NM_s}} \sum_{\lambda \vec{k}} Q_{\lambda \vec{k}} \varepsilon_{\lambda \vec{k}}^\alpha(s) e^{ik(z_l - z_0)}, \quad (8)$$

where N is the number of primitive cells in the crystal. In Eq. (8) the amplitude of each vibrational normal mode $Q_{\lambda \vec{k}}$ is determined by inverse Fourier transform of the function in Eq. (7).

To determine initial atomic velocities we add time dependence to the displacements in Eq. (8) and differentiate with

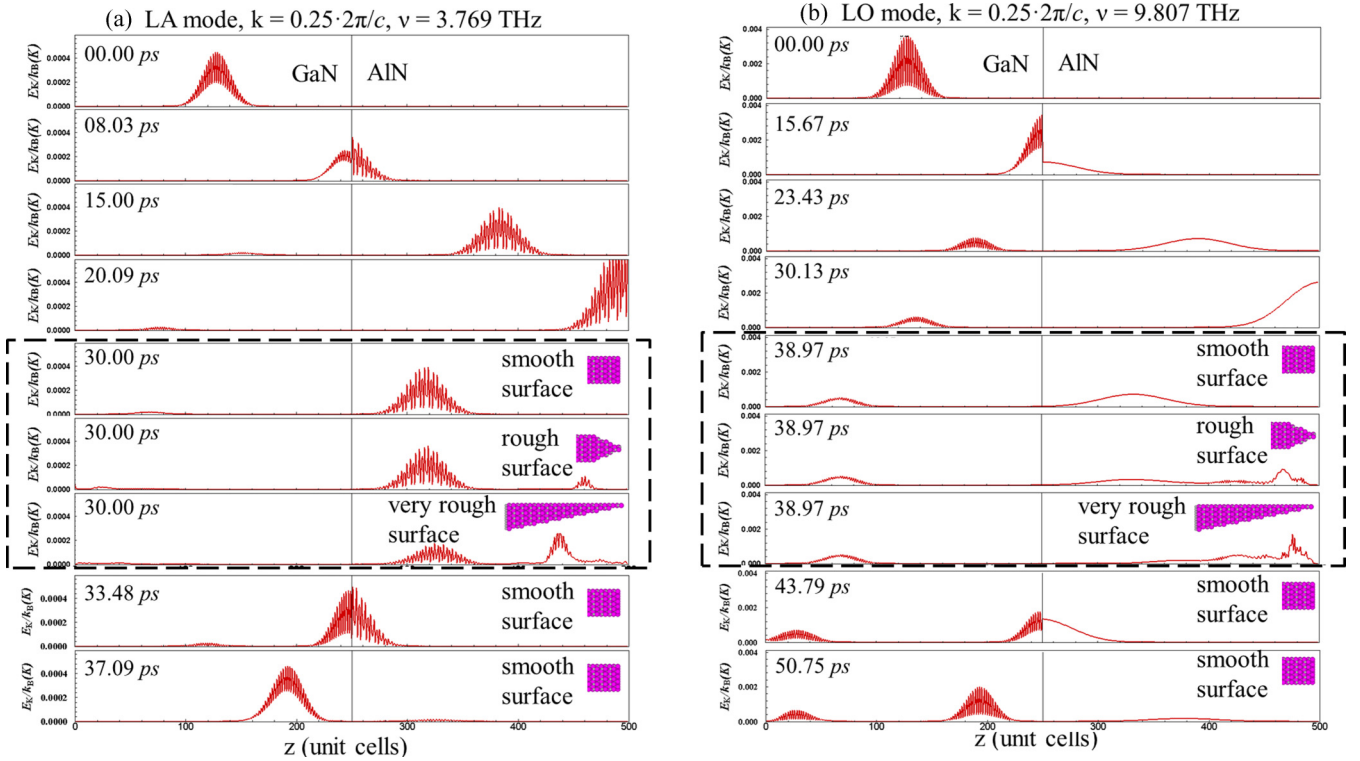


FIG. 9. (Color online) Snapshots of kinetic energy for (a) a LA wave packet with $\nu = 3.769$ THz and (b) a LO wave packet with $\nu = 9.807$ THz. The snapshots in the dashed box demonstrate the kinetic energy of the wave packet after it is scattered by a smooth, rough, and very rough surface.

respect to time. Hence, the initial velocities are given by

$$\dot{u}_l^\alpha(s) = \frac{1}{\sqrt{NM_s}} \sum_{\lambda \vec{k}} -i\omega_{\lambda \vec{k}} Q_{\lambda \vec{k}} \varepsilon_{\lambda \vec{k}}^\alpha(s) e^{ik(z_l - z_0)}, \quad (9)$$

where $\omega_{\lambda k}$ is the eigenvalue for λ branch at k .

To clearly observe the phonon transmission and boundary scattering processes, we use a system size of 250|250 unit cells in the wave packet simulation. The wave packet is launched in the center of the GaN lead. The initial atomic displacements and velocities are given by Eqs. (8) and (9).

Figure 9(a) shows snapshots of the kinetic energy of atoms for a longitudinal-acoustic (LA) wave packet centered at 3.77 THz. The snapshots in the initial 15 ps of the simulation show the phonon transmission across the epitaxial GaN|AlN interface. A large portion of energy is transmitted, and only a small portion of the energy is reflected. By Fourier transform the atomic displacements in the AlN lead after phonon transmission, we find the transmitted wave packet is also a LA wave packet centered at 3.77 THz. Hence, the LA wave packet in GaN scatters elastically into a LA wave packet in AlN at the epitaxial interface. By computing the total energy in the two leads before and after phonon transmission, we find the energy transmission coefficient τ of a LA wave packet centered at 3.77 THz is 0.95.

The transmission coefficient can be also determined by AMM. For phonons arriving normal to the interface, the AMM predicts [30]

$$\tau = \frac{4Z_{\text{GaN}}Z_{\text{AlN}}}{(Z_{\text{GaN}} + Z_{\text{AlN}})^2}, \quad (10)$$

where $Z = \rho c$ is the acoustic impedance of material, ρ is the density, and c is the phonon group velocity. The phonon group velocity is obtained from the slope of dispersion curves shown in Fig. 8. To compare with the above simulation result for a LA wave packet, we estimate c in each material as the LA phonon group velocities in the $k \rightarrow 0$ limit. With these calculated values we find that the transmission coefficient predicted by the AMM is 0.955, which agrees very well with the wave-packet simulation result. Our previous work [20] shows there are a few low- and high-frequency modes localized at the epitaxial GaN|AlN interface. These modes might scatter phonons with similar frequency and lead to a smaller τ , but due to their limited number they should be rather inconsequential for the overall interfacial resistance.

When the wave packet reaches the external surface, phonon-boundary scattering is strongly affected by the surface roughness. As shown in Fig. 9(a), we consider three types of surface roughness: (i) smooth surfaces, (ii) rough surfaces, and (iii) very rough surfaces. The snapshots at 30 ps show the kinetic energy of atoms after the phonon wave packet is scattered by the external surface.

It is evident from Fig. 9(a) that the smooth surface scatters phonons specularly. The magnitude and the shape of the wave packet are conserved after the surface scattering. This is consistent with the prediction from Eq. (2) in the case of surface roughness $h \approx 0$. As h becomes larger, Eq. (2) predicts the surface scattering will be partially diffuse. It is shown in Fig. 9(a) that there is a small wave packet moving much more slowly than the specularly reflected one. This indicates phonons are partially scattered to other modes or

other directions. At the very rough surface, this phenomenon is more evident and a large portion of phonons is scattered diffusely. Moreover, we observe nonzero atomic velocity in the transverse direction after the LA phonon wave packet is scattered by the rough surface. This may indicate the polarization of a portion of phonons is changed after being scattered by the rough surface.

The phonon scattering at external surfaces strongly affects the interfacial phonon transport. As shown in the last two snapshots in Fig. 9(a), without a thermalizing scattering event such as phonon-phonon scattering in the lead material or diffuse scattering at the external surface, phonons can transmit back to GaN lead. In this case, the effective transmission coefficient is very small as shown in the last snapshot of Fig. 9(a). One way to diminish such an effect is to increase the system size to increase the probability of phonon-phonon scattering in the lead material. The other way is to introduce a very rough external surface to diffusely scatter phonons at the external surface. The latter method is obviously more efficient computationally.

Similarly, we show snapshots of the kinetic energy of atoms for a longitudinal-optical (LO) wave packet centered at 9.81 THz in Fig. 9(b). By analyzing snapshots in the initial 23.5 ps, we find the interface scattering of the LO wave packet is an elastic LO→LO scattering process with a transmission coefficient of 0.762. The transmitted wave packet is much wider than the incident one because the group velocity of the 9.81-THz LO phonon in AlN is much larger than that in GaN. The three snapshots at 39 ps in Fig. 9(b) correspond to wave packets scattered by, respectively, a smooth, rough, and very rough external surface. It is evident from Fig. 9(b) that the smooth surface scatters the LO phonon specularly. The rough surface scatters the LO phonon semidiffusely. An essentially diffuse scattering of the LO phonon is found at the very rough surface.

A comparison between Figs. 9(a) and 9(b) shows that with same surface roughness, the scattering of the LO phonon is more diffuse than that of the LA phonon. This is due to the fact that the wavelength (about 1 nm) of the 9.81-THz LO phonon in AlN is much smaller than that (about 3 nm) of the 3.77-THz LA phonon in AlN. According to Eq. (2), a smaller wavelength indicating a greater wave vector k results in a smaller specularity, which means the boundary scattering is more diffuse. This result shows the phonon-boundary scattering is also frequency dependent.

Finally, the snapshots at 43.8 and 50.8 ps in Fig. 9(b) show that if the LO phonon is specularly reflected, a large portion of phonon energy will return to GaN, which results in a reduction in the effective transmission coefficient and an increase of R_K , as was the case for LA phonons.

IV. EMD PREDICTION OF R_K

A. Green-Kubo method

The EMD method evaluates the interfacial thermal conductance via the Green-Kubo formula [41]

$$G_K = \frac{1}{Ak_B T^2} \int_0^\infty \langle P(t)P(0) \rangle dt, \quad (11)$$

where A is the cross section area of interface, and P is the fluctuating heat power across the solid-solid interface which can be computed by

$$P(t) = dE_{\text{lead}}(t)/dt, \quad (12)$$

where E_{lead} is the internal energy of the lead on either side of the interface at time t . In computing G_K at the GaN|AlN interface, we use the internal energy of the AlN lead in Eq. (12). The Green-Kubo relation shown in Eq. (11) is only valid for an infinite system where the heat capacity of the two materials forming the interface $C_V \rightarrow \infty$ [12]. For a finite system, the G_K relates to the long-time integral of $\langle P(t)P(0) \rangle$ by [12]

$$G_K e^{-at_s} = \frac{1}{Ak_B T^2} \int_0^{t_s} \langle P(t)P(0) \rangle dt, \quad (13)$$

where $a = AG_K/C_V$, and t_s is the integration time. Our previous study on EMD prediction of G_K at a solid-gas interface has shown that the exponential decay part of the running integral $\int \langle P(t)P(0) \rangle dt$ is more reliable in the determination of G_K than the value of the initial plateau [14]. We also found that G_K predicted by the EMD method agrees very well with NEMD predictions [14]. In this work, a similar method will be applied to determine G_K at a solid-solid interface.

B. Size effect on EMD prediction of G_K

Using the EMD Green-Kubo method, we first determine G_K at an epitaxial GaN|AlN interface involving smooth external surfaces. The system length is 40|40 unit cells. The thermostat is first applied to equilibrate the system to 300 K. After equilibration, the thermostat is removed and EMD simulation is performed at constant energy in the production run. Data from 30 ns simulation runs are used to compute the autocorrelation function (ACF) of heat power across the GaN|AlN interface. The running integral of ACF is shown in Fig. 10(a). After 2 ps the running integral exhibits a monotonic decay till ~ 15 ps. This behavior is consistent with the prediction of Eq. (13). After 15 ps, however, the running integral exhibits a slower decay mixed with oscillations. It is depicted in Fig. 10(a) that the period of the oscillation is ~ 20 ps. Similar oscillations in the tail of the running integral were also observed by Merabia and Termentzidis in EMD prediction of G_K at an interface between two LJ crystals [15].

We find these oscillations are not caused by statistical errors, but by echoes of phonon reflection from the external surfaces. Using the method described in Sec. III, we estimate the average phonon group velocity $c \approx 5530$ m/s for strained GaN and $c \approx 6700$ m/s for AlN. The total length of the GaN|AlN structure is 41 nm. For phonons traveling normal to the interface, therefore, it takes ~ 13.4 ps to travel back and forth in the structure for one period. Allowing for the longer distance traveled by other phonons in various angles, the 20-ps oscillation period shown in Fig. 10(a) is consistent with the average time period for phonons traveling in the 41-nm long structure.

When the system size increases, it takes a longer time for phonons to travel through the whole structure. Accordingly, the period of oscillations in the tail of the running integral increases from 20 to 39 ps as the system size increases from 40|40 unit cells to 75|75 unit cells as shown in Fig. 10(b).

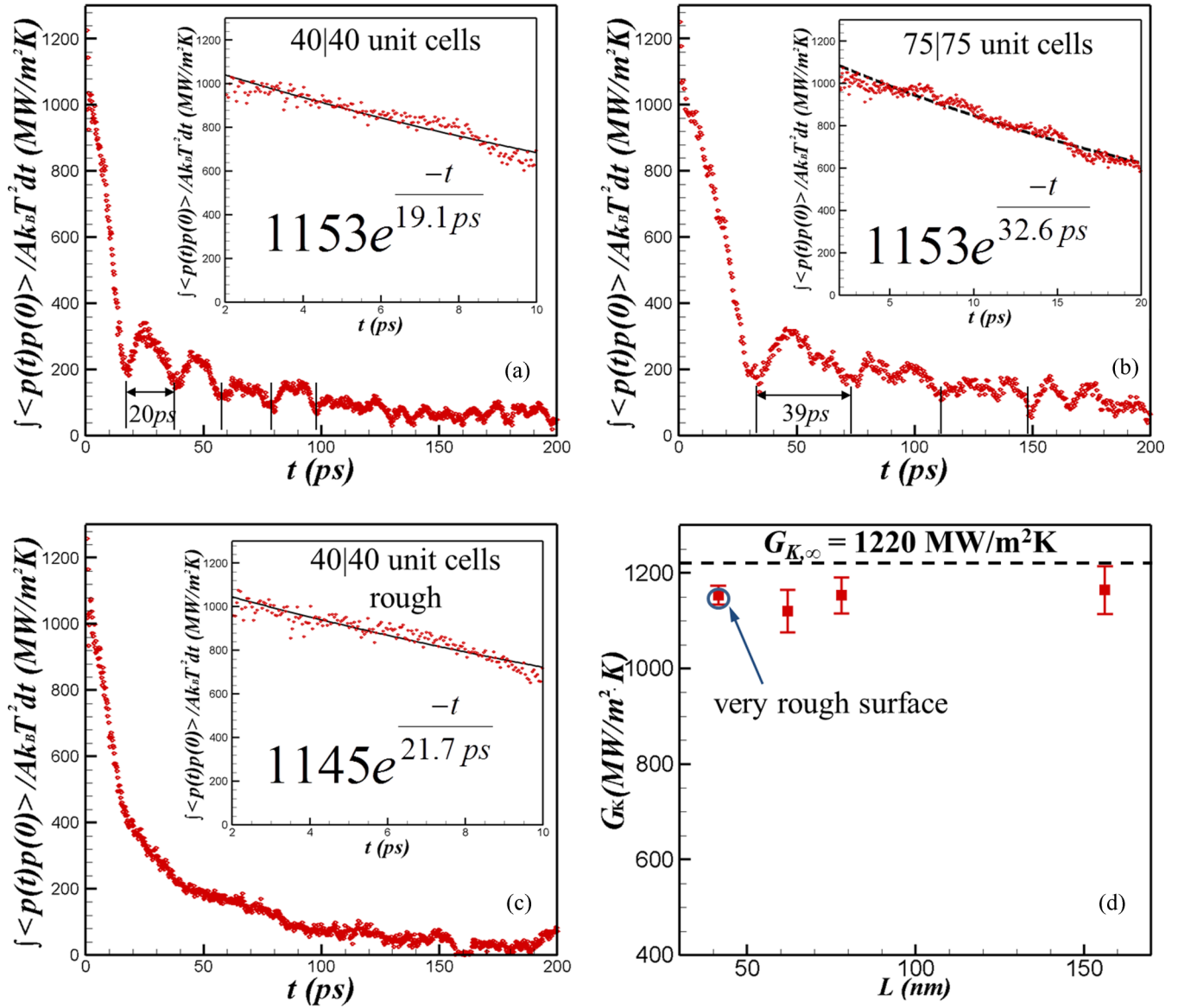


FIG. 10. (Color online) The running integral of time correlation function in (a) 40|40-unit-cell structure involving smooth external surface, (b) 75|75-unit-cell structure involving smooth external surface, and (c) 40|40-unit-cell structure involving very rough external surface. The insets in (a), (b), and (c) show fittings of an exponential function to the initial part of the running integral. (d) EMD prediction of G_K as a function of system length. The horizontal dashed line indicates the value of $G_{K,\infty}$ from NEMD simulation. The uncertainties are determined from the analysis of four independent simulation runs.

In Fig. 10(c) we show the integral of the ACF in the case when the external surfaces are very rough. Very rough surfaces scatter the majority of phonons diffusely, thus greatly suppressing the echoes of phonons. It is shown in Fig. 10(c) that the oscillations in the tail of the running integral essentially disappear when very rough external surfaces are introduced. However, the rate of decay of the ACF integral changes after ~ 20 ps. We attribute this to the finite size effects associated with diffusely scattered phonons at the external boundary returning to the interface.

To obtain G_K from the EMD simulation, therefore, we only use part of the running integral in which neither the echoes nor the lower rate of decay are observed yet. In the inset of Fig. 10(a) we show that the running integral of initial 2 to 10 ps can be well fitted by an exponential function. The running

integral of initial 2 ps is excluded in the fitting due to very large initial oscillations. Using the relation in Eq. (13), the exponential fit gives $G_K \approx 1.15$ GW/m² K, which is close to $G_{K,\infty} \approx 1.22$ GW/m² K from the NEMD method. A similar procedure is applied to determine G_K in a system with larger sizes or with very rough surfaces as shown in Figs. 10(b) and 10(c). The maximum system length used in the simulation is 150|150 unit cells. In all cases, the G_K predicted by the EMD method is close to $G_{K,\infty}$ obtained from the NEMD method as shown in Fig. 10(d).

The above analysis shows that if the finite size effects are treated properly, a size-independent G_K can be predicted from the EMD method, and the G_K predicted by the EMD method is consistent with $G_{K,\infty}$ predicted by the NEMD method.

V. SUMMARY AND CONCLUSIONS

We investigated the finite size effect on MD prediction of R_K at a solid-solid interface. Using NEMD simulation and wave-packet simulations, we demonstrated that the size-dependent R_K obtained from NEMD simulation is mainly caused by the specular reflection of phonons at the smooth external surfaces. Wave-packet simulations demonstrated explicitly that as the roughness of external surfaces increases, phonons are scattered more diffusely at the external surface. Furthermore, by comparing R_K for epitaxial and nonepitaxial interfaces, we demonstrated that the magnitude of size effect on R_K becomes smaller when the interface phonon scattering is more diffuse. Due to the smaller size effect, R_K (nonepitaxial) is larger than R_K (epitaxial) when the system length is long, but smaller than R_K (epitaxial) when the system length is short. Hence, care must be taken when comparing the relative magnitude of R_K at interfaces with different atomic structures and bonding.

We also found that a reliable prediction of $R_{K,\infty}$ in a short-length system cannot be achieved by employing Langevin thermostats in the heat source/sink. Although the Langevin thermostat can scatter phonons diffusely by setting a high friction coefficient, such large friction results in unrealistic

phonon power spectra distributions, which influences the correct prediction of R_K .

Finally, we studied the size effect on EMD predictions of R_K . We found that the oscillations in the tail of the running integral of the time correlation function are caused by the phonon echoes from the smooth external surfaces. In the case of rough external surfaces the oscillations are not presented but the running integral of the time correlation function changes the decay rate when phonons scattered diffusely at the external surfaces return to the interface. In both cases the correct determination of R_K can be achieved by fitting an exponential function to the initial part of the running integral. Using this method we found that the R_K predicted from EMD simulations is size independent and is consistent with $R_{K,\infty}$ obtained from NEMD simulations.

ACKNOWLEDGMENTS

This work is supported by ARL research center: Alliance for the Computationally-guided Design of Energy Efficient Electronic Materials and by the NY State NYSTAR funded Focus Interconnect Center. We would like to thank the National Institute for Computational Science (NICS) for providing us supercomputer resources for MD simulations.

-
- [1] P. L. Kapitza, *J. Phys. (USSR)* **4**, 181 (1941).
 - [2] G. D. Mahan and L. M. Woods, *Phys. Rev. Lett.* **80**, 4016 (1998).
 - [3] X. Zhang, M. Hu, K. P. Giapis, and D. Poulikakos, *J. Heat Transfer* **134**, 102402 (2012).
 - [4] T. Westover, R. Jones, J. Huang, G. Wang, E. Lai, and A. A. Talin, *Nano Lett.* **9**, 257 (2009).
 - [5] Z. Liang and H.-L. Tsai, *J. Phys.: Condens. Matter* **23**, 495303 (2011).
 - [6] T. S. English, J. C. Duda, J. L. Smoyer, D. A. Jordan, P. M. Norris, and L. V. Zhigilei, *Phys. Rev. B* **85**, 035438 (2012).
 - [7] Z. Tian, K. Esfarjani, and G. Chen, *Phys. Rev. B* **86**, 235304 (2012).
 - [8] X. W. Zhou, R. E. Jones, C. J. Kimmer, J. C. Duda, and P. E. Hopkins, *Phys. Rev. B* **87**, 094303 (2013).
 - [9] L. Zhang, P. Keblinski, J.-S. Wang, and B. Li, *Phys. Rev. B* **83**, 064303 (2011).
 - [10] L. Hu, L. Zhang, M. Hu, J.-S. Wang, B. Li, and P. Keblinski, *Phys. Rev. B* **81**, 235427 (2010).
 - [11] Z. Liang and H.-L. Tsai, *Int. J. Heat Mass Transfer* **55**, 2999 (2012).
 - [12] J.-L. Barrat and F. Chiaruttini, *Mol. Phys.* **101**, 1605 (2003).
 - [13] S. Shenogin, P. Keblinski, D. Bedrov, and G. D. Smith, *J. Chem. Phys.* **124**, 014702 (2006).
 - [14] Z. Liang, W. Evans, and P. Keblinski, *Phys. Rev. E* **87**, 022119 (2013).
 - [15] S. Merabia and K. Termentzidis, *Phys. Rev. B* **86**, 094303 (2012).
 - [16] Y. Chalopin, K. Esfarjani, A. Henry, S. Volz, and G. Chen, *Phys. Rev. B* **85**, 195302 (2012).
 - [17] E. S. Landry and A. J. H. McGaughey, *Phys. Rev. B* **80**, 165304 (2009).
 - [18] R. E. Jones, J. C. Duda, X. W. Zhou, C. J. Kimmer, and P. E. Hopkins, *Appl. Phys. Lett.* **102**, 183119 (2013).
 - [19] T. Watanabe, B. Ni, S. R. Phillpot, P. K. Schelling, and P. Keblinski, *J. Appl. Phys.* **102**, 063503 (2007).
 - [20] Z. Liang, K. Sasikumar, and P. Keblinski, *Phys. Rev. Lett.* **113**, 065901 (2014).
 - [21] J. Yang, M. Shen, Y. Yang, W. J. Evans, Z. Wei, W. Chen, A. A. Zinn, Y. Chen, R. Prasher, T. T. Xu, P. Keblinski, and D. Li, *Phys. Rev. Lett.* **112**, 205901 (2014).
 - [22] A. Bere and A. Serra, *Phys. Rev. B* **65**, 205323 (2002).
 - [23] H. P. Lei, Ph.D. thesis, Caen University, France, 2009.
 - [24] D. Frenkel and B. Smit, *Understanding Molecular Simulation* (Academic, San Diego, 2002), p. 75.
 - [25] P. Jund and R. Jullien, *Phys. Rev. B* **59**, 13707 (1999).
 - [26] Y. K. Koh, Y. Cao, D. G. Cahill, and D. Jena, *Adv. Funct. Mater.* **19**, 610 (2009).
 - [27] M. Maldovan, *Appl. Phys. Lett.* **101**, 113110 (2012).
 - [28] P. K. Schelling, S. R. Phillpot, and P. Keblinski, *J. Appl. Phys.* **95**, 6082 (2004).
 - [29] S. Shin, M. Kaviani, T. Desai, and R. Bonner, *Phys. Rev. B* **82**, 081302(R) (2010).
 - [30] E. T. Swartz and R. O. Pohl, *Rev. Mod. Phys.* **61**, 605 (1989).
 - [31] M. E. Levinstein, S. L. Rumyantsev, and M. S. Shur, *Properties of Advanced Semiconductor Materials GaN, AlN, InN, BN, SiC, SiGe* (John Wiley and Sons, New York, 2001), pp. 31–47.
 - [32] S. A. Adelman and J. D. Doll, *J. Chem. Phys.* **64**, 2375 (1976).
 - [33] M. P. Allen and D. J. Tildesley, *Computer Simulation of Liquid* (Oxford University Press, Oxford, 2000).
 - [34] J. C. Nipko, C. K. Loong, C. M. Balkas, and R. F. Davis, *Appl. Phys. Lett.* **73**, 34 (1998).
 - [35] C.-K. Loong, *J. Eur. Ceram. Soc.* **19**, 2241 (1999).

- [36] X. W. Zhou, S. Aubry, R. E. Jones, A. Greenstein, and P. K. Schelling, *Phys. Rev. B* **79**, 115201 (2009).
- [37] N. Shenogina, P. Koblinski, and S. Garde, *J. Chem. Phys.* **129**, 155105 (2008).
- [38] E. S. Landry and A. J. H. McGaughey, *J. Appl. Phys.* **107**, 013521 (2010).
- [39] R. Prasher, *Appl. Phys. Lett.* **94**, 041905 (2009).
- [40] P. K. Schelling, S. R. Phillpot, and P. Koblinski, *Appl. Phys. Lett.* **80**, 2484 (2002).
- [41] L. Puech, G. Bonfait, and B. Castaing, *J. Low Temp. Phys.* **62**, 315 (1986).